Electronic Supplementary Information (ESI)

Temperature- and solvent-induced reversible single-crystal-to-single-crystal transformations of Tb^{III}-based MOFs with excellent stability and fluorescence sensing properties toward drug molecules

Yu Li,‡ Bi-Lian Chai,‡ Hui Xu, Teng-Fei Zheng, Jing-Lin Chen, Sui-Jun Liu* and He-Rui Wen

School of Chemistry and Chemical Engineering, Jiangxi Provincial Key Laboratory of Functional Molecular Materials Chemistry, Jiangxi University of Science and Technology, Ganzhou 341000, Jiangxi Province, P.R. China

*Corresponding author. E-mail: sjliu@jxust.edu.cn (S.-J. Liu). Tel: +86-797-8312204.

‡These authors contributed equally to this work and should be considered co-first authors.

CONTENTS

Section 1. Experimental Section

1. Materials and Instrumentations.

All starting materials including 5,5'-(benzo[c][1,2,5]thiadiazole-4,7-diyl) diisophthalic acid (H_4BTDI) (Scheme S1) were reagent grade and used by the purchase without further purification. The powder X-ray diffraction (PXRD) patterns were recorded on a Rigaku Miniflex 600 instrument. The IR spectra were measured in the range of 4000–400 cm^{-1} with KBr pellets on a Bruker Alpha FT-IR spectrometer. Thermogravimetric analysis (TGA) was carried out on a NETZSCH STA2500 (TG/DTA) thermal analyzer under a N_2 flow at a heating rate of 10 °C min^{-1}. Fluorescence spectra were obtained using a F4600 (Hitachi) FL spectrophotometer. The ultraviolet visible (UV-vis) absorption spectra were collected on a UV-vis 2550 spectrophotometer. The calculation of H_4BTDI and fleroxacin (FO) based on density functional theory was implemented by using GaussView 6.0. Elemental analysis (C, H, N and S) was performed on a vario EL cube elemental analyzer.

2. Crystallographic studies for JXUST-12, JXUST-12a and JXUST-12'.

Single-crystal X-ray diffraction data were obtained on a Bruker D8 QUEST diffractometer with Mo-Kα radiation (λ = 0.71073 Å) using ω scan mode. The SAINT program was used for integration of the diffraction profiles.[S1] The structures were solved with direct methods and refined by using full-matrix least squares on F^2 with SHELXL-2017/1.[S2] All non-H atoms were confirmed by successive difference Fourier syntheses and treated isotropically. Moreover, all hydrogen atoms were calculated in idealized positions on a geometric basis and refined with restrictions. Because of the limited crystal quality, the hydrogen atoms of O3W and O4W (**JXUST-12a**) were not assigned and the positions of the corresponding hydrogen atoms of O2W could not be clearly localized. In addition, the solvent molecules in **JXUST-12a** could not be determined reasonably, which were squeezed *via* SQUEEZE program of PLATON[S3] software owing to the high disordering. The summary of the crystal data and structural refinements of **JXUST-12**, **JXUST-12a** and **JXUST-12'** is provided in Table S1 (ESI). Selected bond lengths and bond angles of **JXUST-12**, **JXUST-12a** and **JXUST-12'** are listed in Table S2-S4 (ESI).

Ref.

S1 *SAINT*, *Version 6.02a*, Bruker AXS Inc, Madison, WI, 2002.

S2 G. M. Sheldrick, *Acta Crystallogr. Sect. A: Found. Adv.,* 2015, **A71**, 3−8.

S3 A. L. Spek, *Acta Crystallogr, Sect. C: Struct. Chem.,* 2015, **C71**, 9−18.

Section 2. Supplementary Tables, Scheme and Structural Figures

Table S1. Crystal data and structure refinements for **JXUST-12**, **JXUST-12a** and **JXUST-12'**.

Compound	**JXUST-12**	**JXUST-12a**	**JXUST-12'**
formula	$C_{78}H_{50}N_{10}O_{28}S_3Tb_4$	$C_{66}H_{30}N_6O_{32}S_3Tb_4$	$C_{78}H_{50}N_{10}O_{28}S_3Tb_4$
*M*r	2307.14	2150.82	2307.14
T (K)	296(2)	296(2)	295(2)
crystal system	triclinic	triclinic	triclinic
space group	$P\bar{1}$	$P\bar{1}$	$P\bar{1}$
a (Å)	10.9195(4)	10.9806(9)	10.9612(11)
b (Å)	12.0091(4)	11.2912(11)	11.9435(12)
c (Å)	15.8371(5)	15.8685(13)	15.8769(16)
α (º)	73.442(1)	104.446(3)	73.728(3)
β (º)	70.805(1)	109.909(2)	70.543(2)
γ (º)	86.913(1)	90.567(3)	87.158(3)
V (Å^3)	1878.16(11)	1781.6(3)	1879.1(3)
Z	1	1	1
F(000)	1120	1032	1120
D_{calc} (g cm^{-3})	2.040	2.005	2.039
μ (mm^{-1})	3.899	4.105	3.897
Collected reflections	28294	20932	19152
Unique reflections	8529	6224	6531
R_{int}	0.0336	0.0371	0.0305
R_1[a]/wR_2[b] [$I>2\sigma(I)$]	0.0457/0.1004	0.0612/0.1426	0.0690/0.1591
R_1[a]/wR_2[b] (all data)	0.0604/0.1078	0.0717/0.1510	0.0805/0.1693
GOF on F^2	1.041	1.175	1.019

[a]$R_1 = \Sigma(||F_0| - |F_C||)/\Sigma|F_0|$. [b]$wR_2 = [\Sigma w(|F_0|^2 - |F_C|^2)^2/(\Sigma w|F_0|^2)^2]^{1/2}$.

Table S2. Selected bond lengths (Å) and angles (°) for **JXUST-12**[a].

Tb1—O13	2.247(5)	Tb2—O3	2.243(5)
Tb1—O10^{ii}	2.255(5)	Tb2—O5	2.271(5)
Tb1—O1	2.256(6)	Tb2—O11^{ii}	2.275(5)
Tb1—O17	2.369(7)	Tb2—O18	2.323(6)
Tb1—O7^{iii}	2.376(5)	Tb2—O4^{iv}	2.332(4)
Tb1—O6^{iii}	2.434(5)	Tb2—O8^{v}	2.344(5)
Tb1^{i}—O2	2.336(5)	Tb2—O9^{v}	2.428(5)
O13—Tb1—O10^{ii}	85.98(18)	O3—Tb2—O5	87.65(19)
O13—Tb1—O1	78.6(2)	O3—Tb2—O11^{ii}	83.3(2)
O10^{ii}—Tb1—O1	97.2(2)	O5—Tb2—O11^{ii}	84.65(17)
O13—Tb1—O2^{i}	86.10(18)	O3—Tb2—O18	156.6(2)
O10^{ii}—Tb1—O2^{i}	161.4(2)	O5—Tb2—O18	100.9(2)
O1—Tb1—O2^{i}	97.7(2)	O11^{ii}—Tb2—O18	76.0(2)
O13—Tb1—O17	80.0(2)	O3—Tb2—O4^{iv}	89.07(18)
O10^{ii}—Tb1—O17	85.9(2)	O5—Tb2—O4^{iv}	169.88(16)
O1—Tb1—O17	158.1(2)	O11^{ii}—Tb2—O4^{iv}	85.46(17)
O2^{i}—Tb1—O17	76.2(2)	O18—Tb2—O4^{iv}	78.75(19)
O13—Tb1—O7^{iii}	156.40(19)	O3—Tb2—O8^{v}	89.31(19)
O10^{ii}—Tb1—O7^{iii}	104.45(19)	O5—Tb2—O8^{v}	114.57(18)
O1—Tb1—O7^{iii}	120.0(2)	O11^{ii}—Tb2—O8^{v}	159.17(18)
O2^{i}—Tb1—O7^{iii}	77.45(19)	O18—Tb2—O8^{v}	106.4(2)
O17—Tb1—O7^{iii}	79.8(2)	O4^{iv}—Tb2—O8^{v}	74.94(18)
O13—Tb1—O6^{iii}	149.28(19)	O3—Tb2—O9^{v}	123.5(2)
O10^{ii}—Tb1—O6^{iii}	77.0(2)	O5—Tb2—O9^{v}	74.73(18)
O1—Tb1—O6^{iii}	78.4(2)	O11^{ii}—Tb2—O9^{v}	144.45(19)
O2^{i}—Tb1—O6^{iii}	116.96(18)	O18—Tb2—O9^{v}	79.8(2)
O17—Tb1—O6^{iii}	123.3(2)	O4^{iv}—Tb2—O9^{v}	114.93(18)
O7^{iii}—Tb1—O6^{iii}	54.24(17)	O8^{v}—Tb2—O9^{v}	54.14(17)

[a]Symmetry codes: (i) -*x*, -*y*+1, -*z*+1; (ii) *x*, *y*, *z*-1; (iii) *x*-1, *y*, *z*; (iv) -*x*+1, -*y*+1, -*z*; (v) *x*+1, *y*, *z*-1.

Table S3. Selected bond lengths (Å) and angles (°) for **JXUST-12a**[b].

Tb1—O1	2.231(9)	Tb2—O9	2.237(10)
Tb1—O8^{ii}	2.244(7)	Tb2—O7^{ii}	2.263(7)
Tb1—O11	2.320(11)	Tb2—O2	2.270(9)
Tb1—O1W	2.339(11)	Tb2—O2W	2.317(11)
Tb1—O5^{iii}	2.407(9)	Tb2—O10^{iv}	2.327(8)
Tb1—O6^{iii}	2.441(8)	Tb2—O4^{v}	2.364(7)
Tb1—O11^{i}	2.692(9)	Tb2—O3^{v}	2.470(7)
Tb1^{i}—O12	2.385(9)	O1W—Tb1—O11^{i}	124.6(3)
O1—Tb1—O8^{ii}	89.0(3)	O12^{i}—Tb1—O11^{i}	50.3(3)
O1—Tb1—O11	92.9(4)	O5^{iii}—Tb1—O11^{i}	72.3(3)
O8^{ii}—Tb1—O11	79.3(4)	O6^{iii}—Tb1—O11^{i}	77.8(3)
O1—Tb1—O1W	77.4(4)	O9—Tb2—O7^{ii}	89.2(3)
O8^{ii}—Tb1—O1W	81.6(4)	O9—Tb2—O2	82.5(4)
O11—Tb1—O1W	158.7(3)	O7^{ii}—Tb2—O2	86.1(3)
O1—Tb1—O12^{i}	155.7(4)	O9—Tb2—O2W	159.0(3)
O8^{ii}—Tb1—O12^{i}	84.5(3)	O7^{ii}—Tb2—O2W	96.5(4)
O11—Tb1—O12^{i}	108.8(3)	O2—Tb2—O2W	77.7(4)
O1W—Tb1—O12^{i}	78.5(4)	O9—Tb2—O10^{iv}	89.9(3)
O1—Tb1—O5^{iii}	100.4(4)	O7^{ii}—Tb2—O10^{iv}	170.7(3)
O8^{ii}—Tb1—O5^{iii}	155.0(3)	O2—Tb2—O10^{iv}	84.6(3)
O11—Tb1—O5^{iii}	122.8(3)	O2W—Tb2—O10^{iv}	81.2(3)
O1W—Tb1—O5^{iii}	78.1(4)	O9—Tb2—O4^{v}	90.2(3)
O12^{i}—Tb1—O5^{iii}	77.4(3)	O7^{ii}—Tb2—O4^{v}	115.5(3)
O1—Tb1—O6^{iii}	76.9(3)	O2—Tb2—O4^{v}	157.2(3)
O8^{ii}—Tb1—O6^{iii}	151.3(3)	O2W—Tb2—O4^{v}	105.3(3)
O11—Tb1—O6^{iii}	76.6(4)	O10^{iv}—Tb2—O4^{v}	73.8(3)
O1W—Tb1—O6^{iii}	118.6(4)	O9—Tb2—O3^{v}	121.7(3)
O12^{i}—Tb1—O6^{iii}	118.0(3)	O7^{ii}—Tb2—O3^{v}	73.8(3)
O5^{iii}—Tb1—O6^{iii}	53.6(3)	O2—Tb2—O3^{v}	147.4(3)
O1—Tb1—O11^{i}	152.6(3)	O2W—Tb2—O3^{v}	79.3(3)
O8^{ii}—Tb1—O11^{i}	108.8(3)	O10^{iv}—Tb2—O3^{v}	114.3(3)
O11—Tb1—O11^{i}	71.1(4)	O4^{v}—Tb2—O3^{v}	53.0(3)

[b]Symmetry codes: (i) -*x*, -*y*+1, -*z*-1; (ii) *x*-1, *y*, *z*-1; (iii) *x*, *y*, *z*-1; (iv) -*x*, -*y*+1, -*z*; (v) *x*-1, *y*, *z*.

Table S4. SHAPE analysis of Tb^{III} ions in **JXUST-12**.

ions	label	shape	symmetry	distortion(τ)
Tb1	HP-7	Heptagon	D_{7h}	29.934
	HPY-7	Hexagonal pyramid	C_{6v}	20.175
	PBPY-7	Pentagonal bipyramid	D_{5h}	4.724
	COC-7	Capped octahedron	C_{3v}	2.366
	CTPR-7	**Capped trigonal prism**	$\boldsymbol{C_{2v}}$	**1.729**
	JPBPY-7	Johnson pentagonal bipyramid J13	D_{5h}	8.005
	JETPY-7	Johnson elongated triangular pyramid J7	C_{3v}	16.888
Tb2	HP-7	Heptagon	D_{7h}	33.235
	HPY-7	Hexagonal pyramid	C_{6v}	19.632
	PBPY-7	Pentagonal bipyramid	D_{5h}	6.418
	COC-7	Capped octahedron	C_{3v}	1.823
	CTPR-7	**Capped trigonal prism**	$\boldsymbol{C_{2v}}$	**1.667**
	JPBPY-7	Johnson pentagonal bipyramid J13	D_{5h}	9.768
	JETPY-7	Johnson elongated triangular pyramid J7	C_{3v}	18.405

Table S5. SHAPE analysis of Tb^{III} ions in **JXUST-12a**.

ions	label	shape	symmetry	distortion(τ)
Tb1	OP-8	Octagon	D_{8h}	33.372
	HPY-8	Heptagonal pyramid	C_{7v}	21.390
	HBPY-8	Hexagonal bipyramid	D_{6h}	14.986
	CU-8	Cube	O_h	9.743
	SAPR-8	**Square antiprism**	$\boldsymbol{D_{4d}}$	**2.301**
	TDD-8	Triangular dodecahedron	D_{2d}	3.037
	JGBF-8	Johnson gyrobifastigium J26	D_{2d}	14.230
	JETBPY-8	Johnson elongated triangular bipyramid J14	D_{3h}	28.147
	JBTPR-8	Biaugmented trigonal prism J50	C_{2v}	3.467
	BTPR-8	Biaugmented trigonal prism	C_{2v}	2.952
	JSD-8	Snub diphenoid J84	D_{2d}	5.488
	TT-8	Triakis tetrahedron	T_d	10.186
	ETBPY-8	Elongated trigonal bipyramid	D_{3h}	23.433
Tb2	HP-7	Heptagon	D_{7h}	32.082
	HPY-7	Hexagonal pyramid	C_{6v}	19.702
	PBPY-7	Pentagonal bipyramid	D_{5h}	5.840
	COC-7	Capped octahedron	C_{3v}	2.343
	CTPR-7	**Capped trigonal prism**	$\boldsymbol{C_{2v}}$	**1.563**
	JPBPY-7	Johnson pentagonal bipyramid J13	D_{5h}	9.115
	JETPY-7	Johnson elongated triangular pyramid J7	C_{3v}	17.919

Table S6. The luminescence sensors with turn-on/turn-off effect based on some selected MOFs.

Analyte	MOF	medium	luminescence effect	K_{sv} (M^{-1})/ K_{ec} (M^{-1})	LOD (μM)	Ref.
NFT	$\{[Tb_4(BTDI)_3(H_2O)_4]\cdot 4H_2O\cdot solvents\}_n$	H_2O	Turn-off	1.74×10^5	0.39	This Work
	$\{[Mg_2(APDA)_2(H_2O)_3]\cdot 5DMA\cdot 5H_2O\}_n$	H_2O		8.82×10^4	0.53	[S4]
	$\{[Tb_4(BTDI)_3(H_2O)_4]\cdot 4H_2O\cdot solvents\}_n$	EtOH		1.34×10^5	0.44	This Work
	$[Tb_4(BTDI)_3(DMF)_4]_n$	EtOH		4.36×10^4	0.86	This Work
	$\{[NaCd_2(L)(BDC)_{2.5}]\cdot 9H_2O\}_n$	DMF		3.57×10^4	1.15	[S5]
NZF	$\{[Tb_4(BTDI)_3(H_2O)_4]\cdot 4H_2O\cdot solvents\}_n$	H_2O	Turn-off	1.43×10^5	0.43	This Work
	$\{[Mg_2(APDA)_2(H_2O)_3]\cdot 5DMA\cdot 5H_2O\}_n$	H_2O		9.0×10^4	0.55	[S4]
	$\{[Tb_4(BTDI)_3(H_2O)_4]\cdot 4H_2O\cdot solvents\}_n$	EtOH		1.04×10^5	0.40	This Work
	$[Tb_4(BTDI)_3(DMF)_4]_n$	EtOH		4.33×10^4	0.82	This Work
	$\{[Cd_3(TDCPB)\cdot 2DMAc]\cdot DMAc\cdot 4H_2O\}_n$	DMF		7.46×10^4	-----	[S6]
DCN	$\{[Tb_4(BTDI)_3(H_2O)_4]\cdot 4H_2O\cdot solvents\}_n$	EtOH	Turn-off	1.23×10^5	0.34	This Work
	$[Tb_4(BTDI)_3(DMF)_4]_n$	EtOH		4.75×10^4	0.88	This Work
	$\{[Zn_2(bpdc)_2(BPyTPE)]\}_n$	CH_2Cl_2		-----	0.63	[S7]
	$\{[Zn_2(L)_2(TPA)]\cdot 2H_2O\}_n$	CH_3OH		2.36×10^4	1.90	[S8]
OFX	$\{[Tb_4(BTDI)_3(H_2O)_4]\cdot 4H_2O\cdot solvents\}_n$	H_2O	Turn-on and blue shift	5.11×10^3	7.34	This Work
	$\{[Zn(TIPA)pim_{0.5}]2H_2O\cdot NO_3\}_n$	DMF	Turn-off	4.61×10^4	-----	[S9]
FO	$\{[Tb_4(BTDI)_3(H_2O)_4]\cdot 4H_2O\cdot solvents\}_n$	H_2O	Turn-on and blue shift	6.03×10^3	2.28	This Work
	$Eu^{3+}@[(Me)_4N]_2[Pb_6K_6(m\text{-}BDC)_9(OH)_2]\cdot H_2O$	H_2O	Turn-on	-----	0.12	[S10]

Ref.

S4 N. Xu, Q.-H. Zhang, B.-S. Hou, Q. Cheng and G.-A. Zhang, A novel magnesium metal-organic framework as a multirespon-sive luminescent sensor for Fe(III) ions, pesticides, and antibiotics with high selectivity and sensitivity, *Inorg. Chem.*, 2018, **57**, 13330-13340.

S5 D. Zhao, X.-H. Liu, Y. Zhao, P. Wang, Y. Liu, M. Azam, S. I. Al-Resayes, Y. Lu and W.-Y. Sun, Luminescent Cd(II)-organic frameworks with chelating NH_2 sites for selective detection of Fe(III) and antibiotics, *J. Mater. Chem. A*, 2017, **5**, 15797-15807.

S6 Q.-Q. Zhu, Q.-S. Zhou, H.-W. Zhang, W.-W. Zhang, D.-Q. Lu, M.-T. Guo, Y. Yuan, F. Sun

and H. He, Design and construction of a metal-organic framework as an efficient luminescent sensor for detecting antibiotics, *Inorg. Chem.*, 2020, **59**, 1323-1331.

S7 C.-L. Tao, B. Chen, X.-G. Liu, L.-J. Zhou, X.-L. Zhu, J. Cao, Z.-G. Gu, Z.-J. Zhao, L. Shen and B.-Z. Tang, A highly luminescent entangled metal-organic framework based on pyridine-substituted tetraphenylethene for efficient pesticide detection, *Chem. Commun.*, 2017, **53**, 9975-9978.

S8 X.-Y. Guo, Z.-P. Dong, F. Zhao, Z.-L. Liu and Y.-Q. Wang, Zinc(II)-organic framework as a multi-responsive photoluminescence sensor for efficient and recyclable detection of pesticide 2,6-dichloro4-nitroaniline, Fe(III) and Cr(VI), *New J. Chem.*, 2019, **43**, 2353-2361.

S9 X.-Q. Yao, G.-B. Xiao, H. Xie, D.-D. Qin, H.-C. Ma, J.-C. Liu, and P.-J. Yan, Solvent-inducted structural diversity of two luminescent metal-organic frameworks as dual-functional sensor for the detection of nitroaromatic compounds and highly selective detection of ofloxacin antibiotics, *CrystEngComm*, 2019, **21**, 2559-2570.

S10 T.-Y. Liu, X.-L. Qua and B. Yan, A highly sensitive and selective “turn-on” fluorescent probe for detection of fleroxacin in human serum and urine based on a lanthanide functionalized metal-organic framework, *Dalton Trans.*, 2019, **48**, 17945-17952.

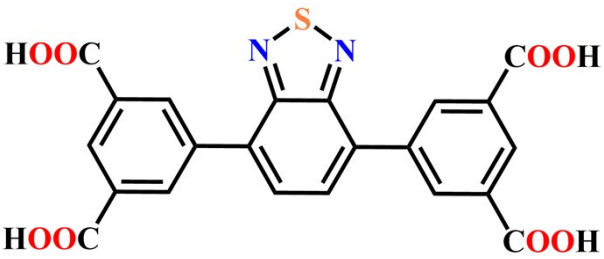

Scheme S1. The structure of H_4BTDI ligand.

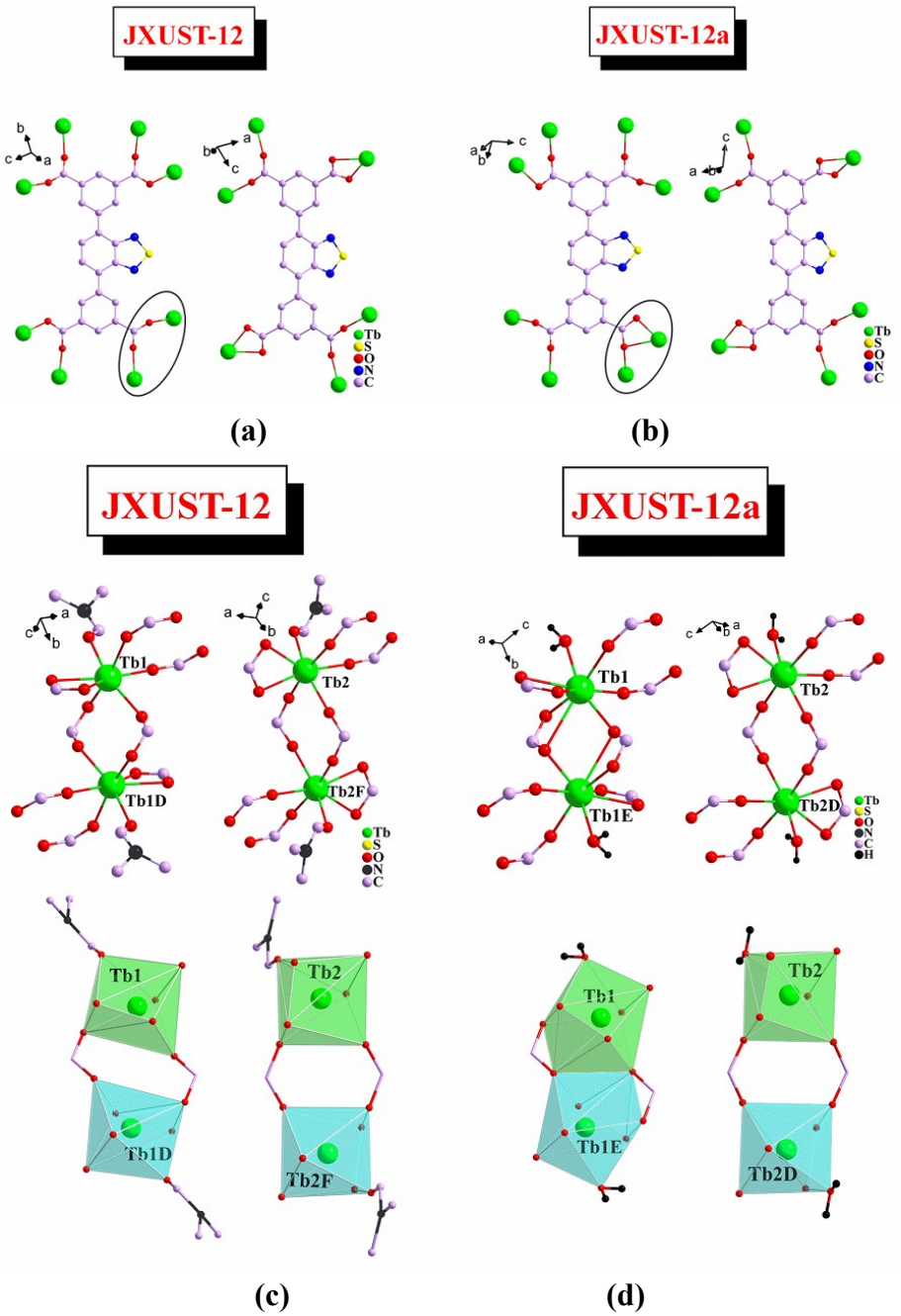

Fig. S1. The coordination modes of $BTDI^{4-}$ ligands in **JXUST-12** (a) and **JXUST-12a** (b), and the coordination configurations of Tb^{III} ions in **JXUST-12** (c) and **JXUST-12a** (d).

Section 3. Supplementary Characterizations

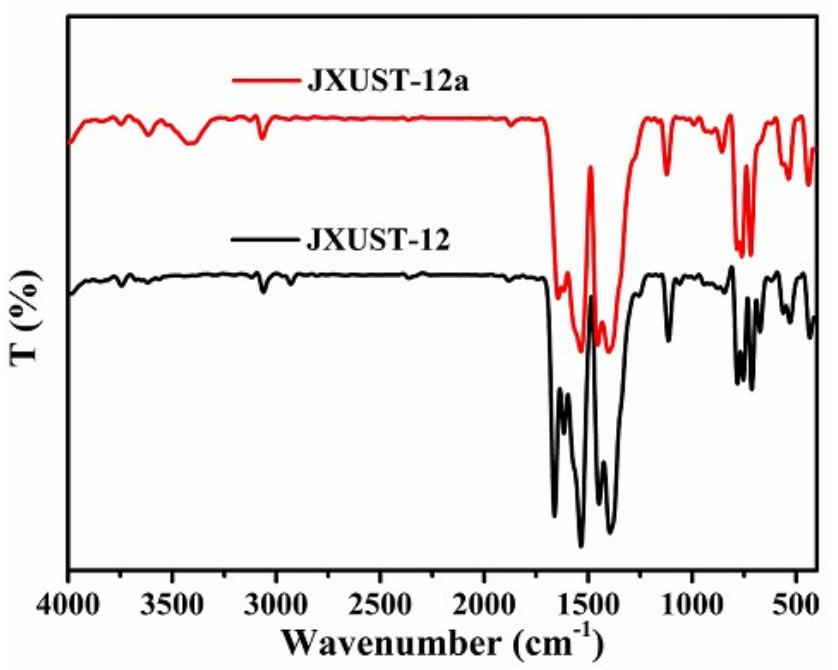

Fig. S2. IR spectra of **JXUST-12** and **JXUST-12a**.

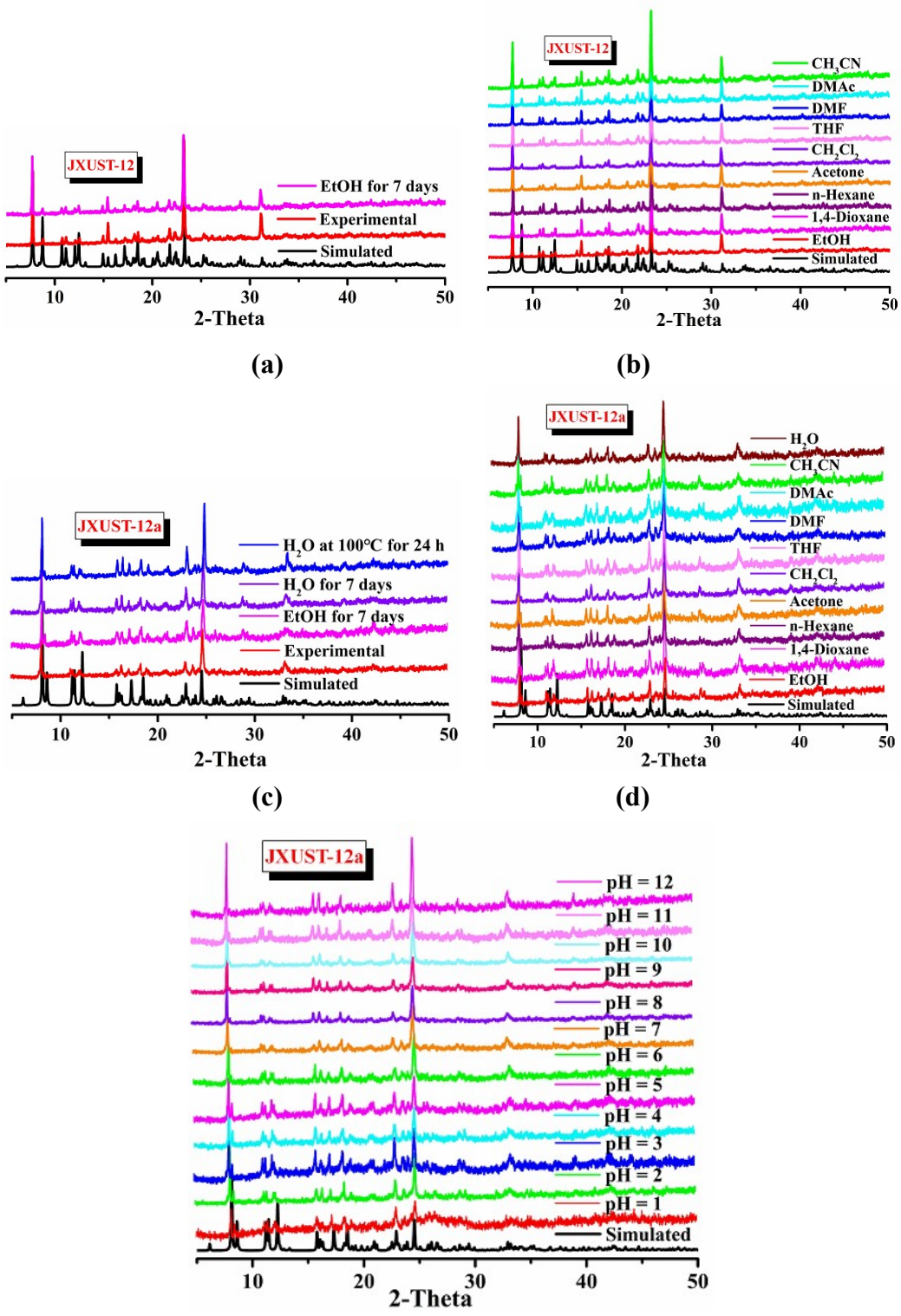

Fig. S3. The simulated and experimental PXRD patterns of as-synthesized samples and the samples soaked in common solvents for **JXUST-12** (a, b) and **JXUST-12a** (c, d). The PXRD patterns of **JXUST-12a** in aqueous solution with different pH values (e).

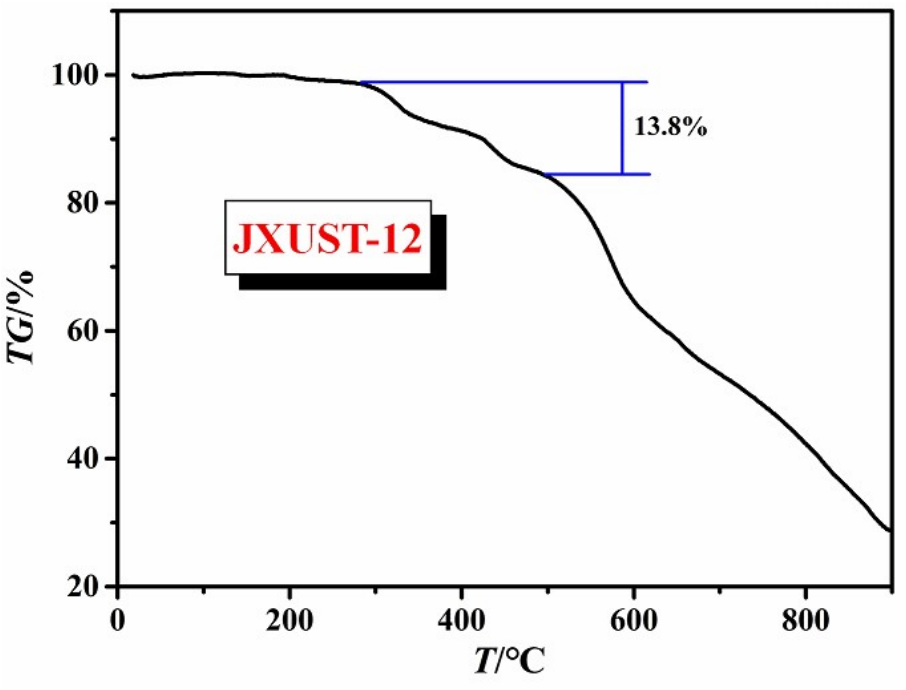

(a)

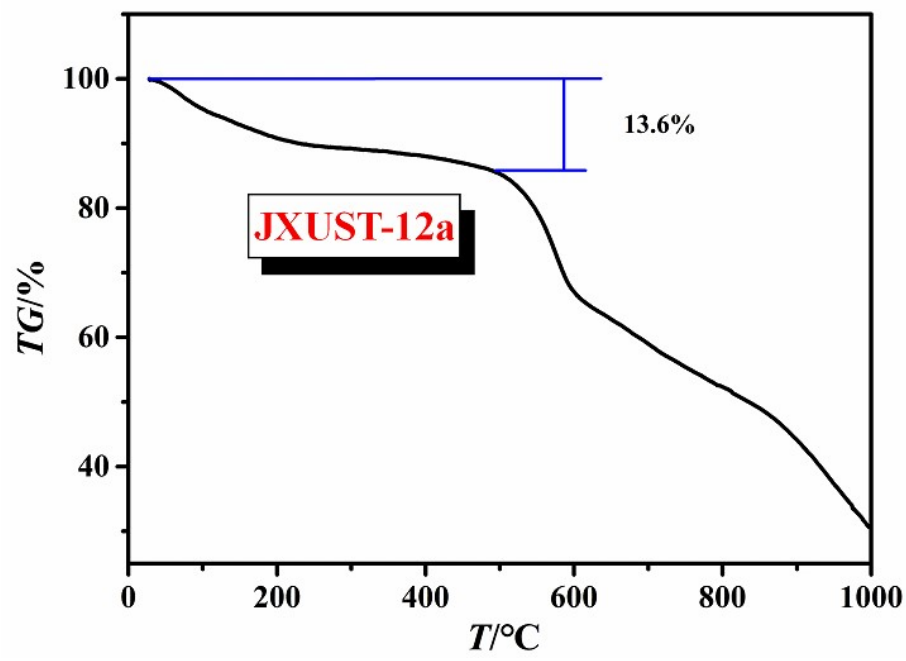

(b)

Fig. S4. The TGA curves for **JXUST-12** (a) and **JXUST-12a** (b).

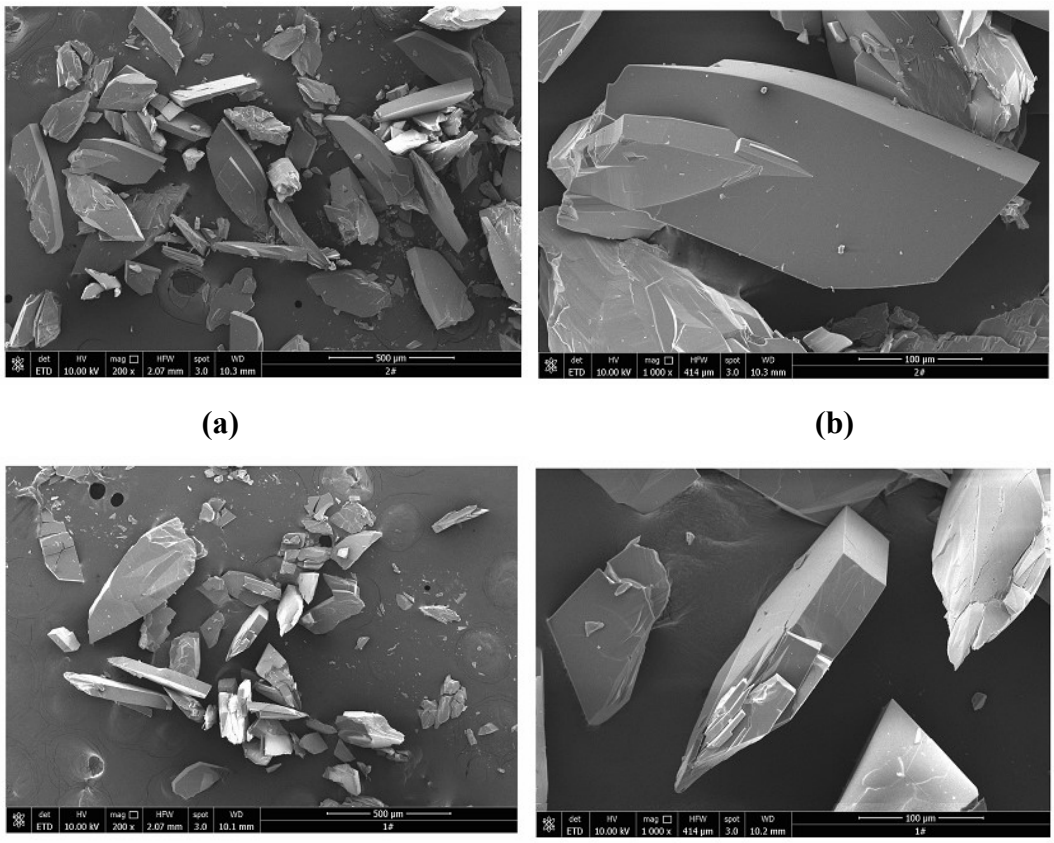

Fig. S5. SEM images of **JXUST-12** (a) and **JXUST-12a** (c). Local SEM images of **JXUST-12** (b) and **JXUST-12a** (d).

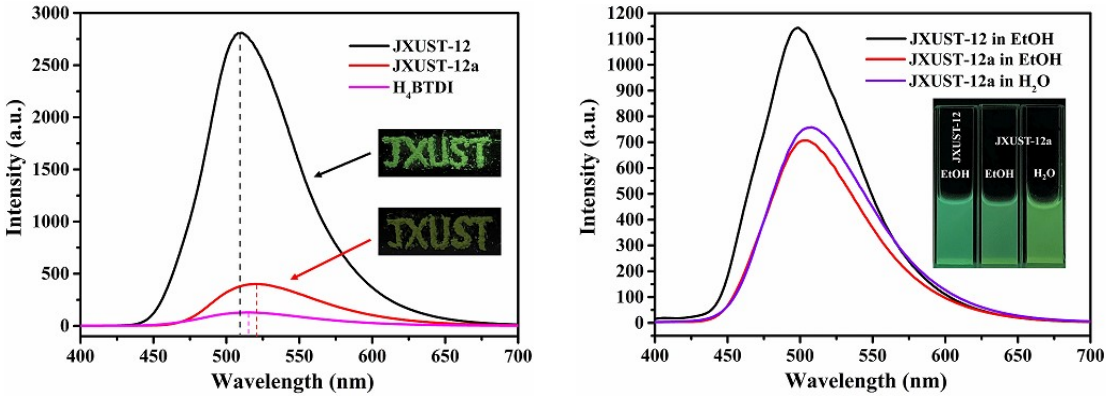

Fig. S6. (a) The emission spectra of H_4BTDI, **JXUST-12** and **JXUST-12a** (λ_{ex} = 370 nm) in the solid state (Inset: the photographs of **JXUST-12** and **JXUST-12a** in the solid state); (b) The emission spectra of H_4BTDI, **JXUST-12** and **JXUST-12a** (λ_{ex} = 370 nm) in different solutions (Inset: the photographs of **JXUST-12** and **JXUST-12a** in different solutions under 365 nm UV-lamp).

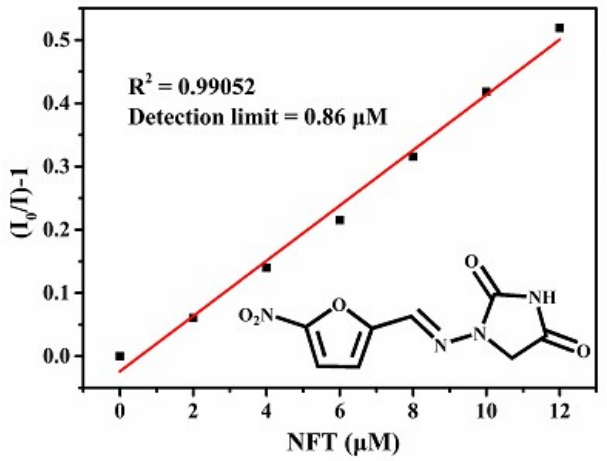

(a)

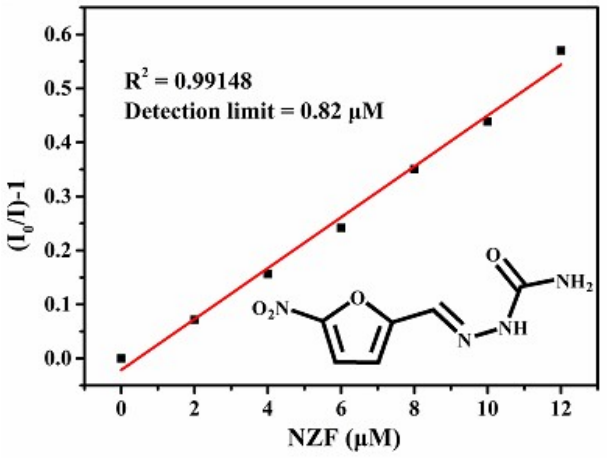

(b)

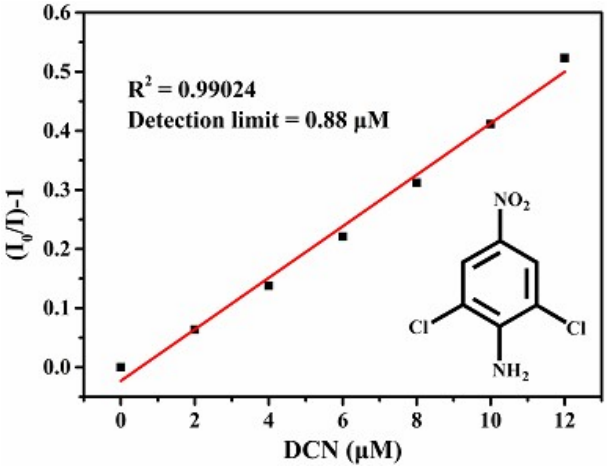

(c)

Fig. S7. The linear relationships between the fluorescence intensities of **JXUST-12** and the concentrations of NFT (a), NZF (b) and DCN (c) in EtOH solution.

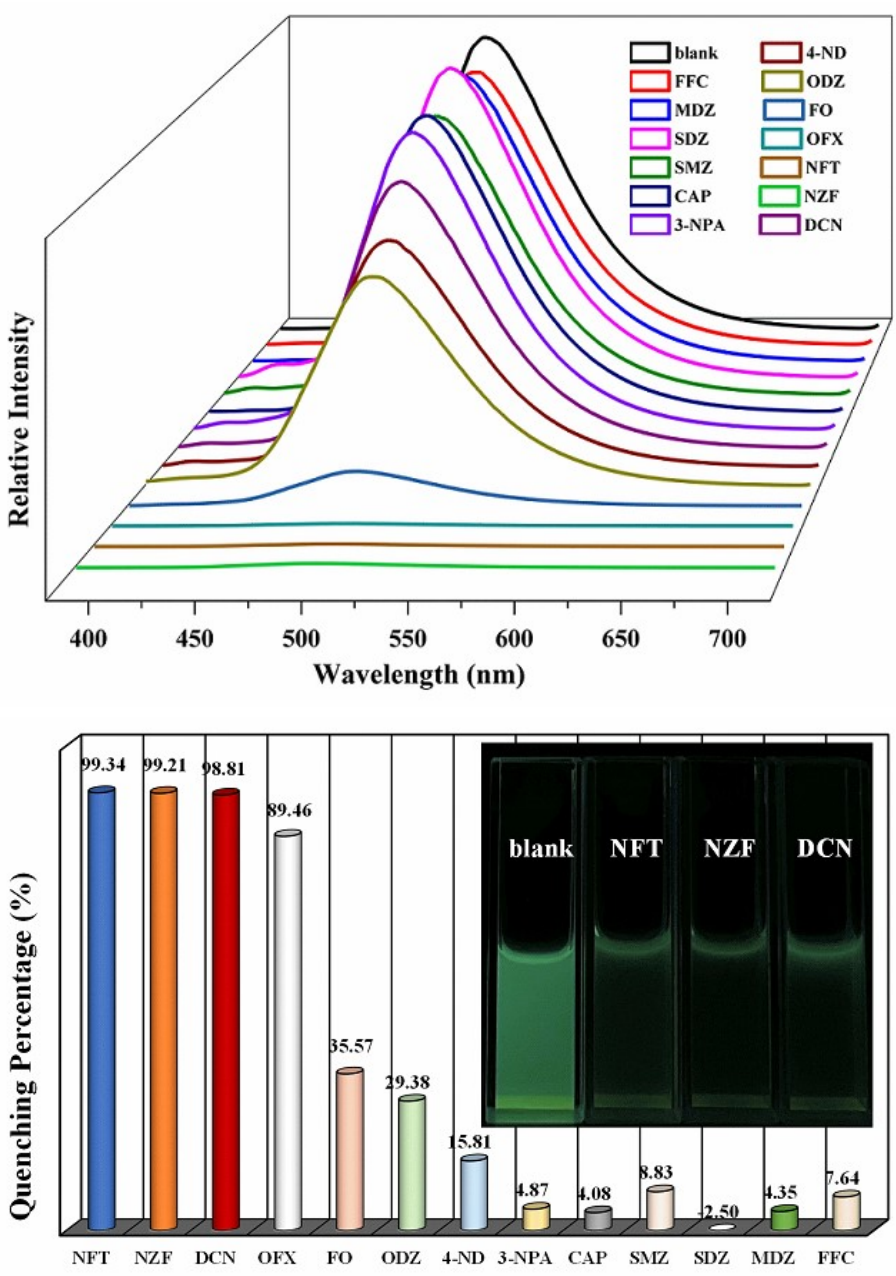

(a)

(b)

Fig. S8. (a) Emission spectra and (b) quenching efficiencies of **JXUST-12a** dispersed in EtOH solution containing different drugs molecules. Inset: the photographs of **JXUST-12a** dispersed in EtOH solution containing NFT, NZF and DCN under 365 nm UV-lamp.

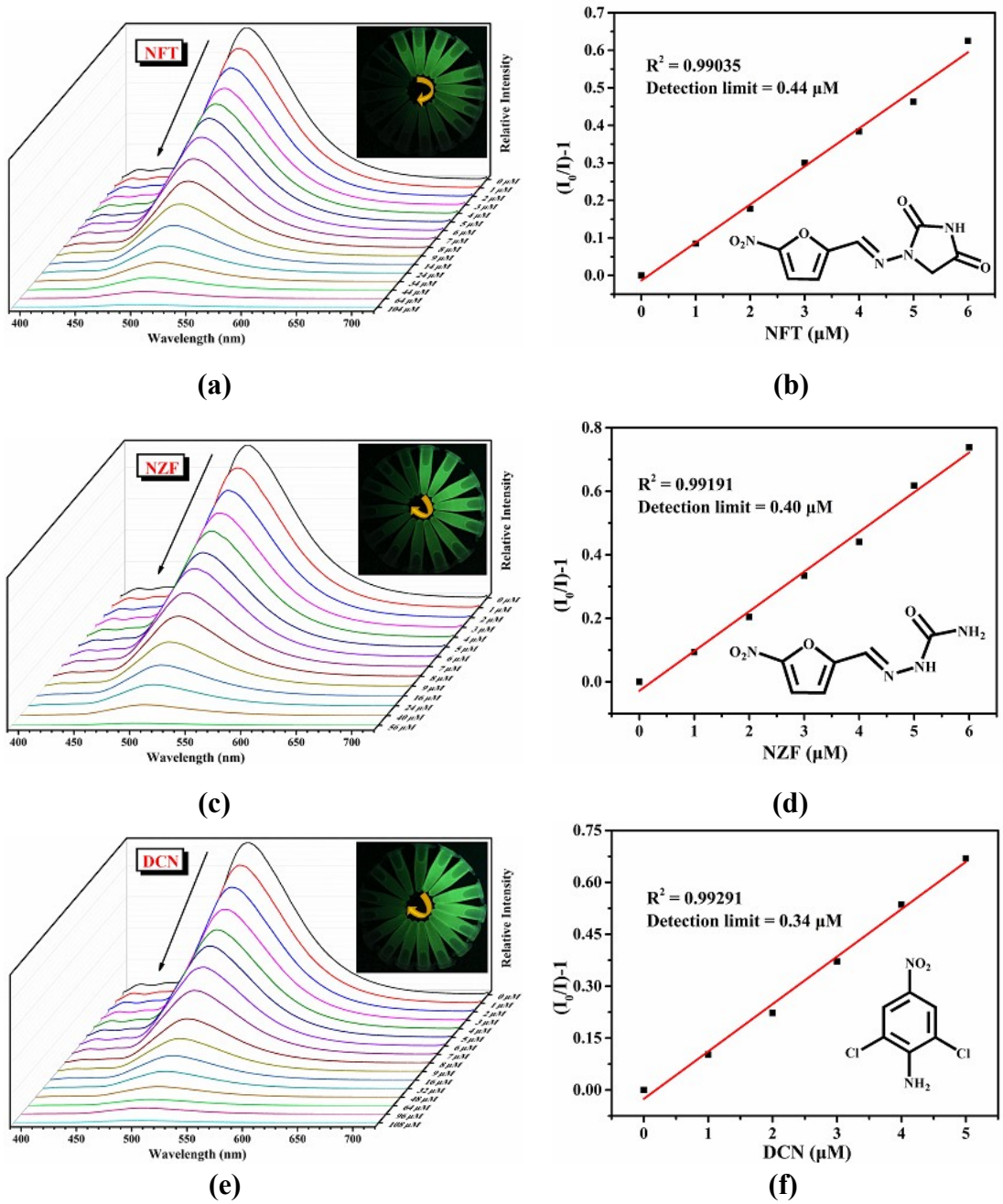

Fig. S9. The emission spectra of **JXUST-12a** dispersed in EtOH solution with various concentrations of NFT (a), NZF (c) and DCN (e), and the linear relationships between the fluorescence intensities of **JXUST-12a** and the concentrations of NFT (b), NZF (d) and DCN (f) in EtOH solution.

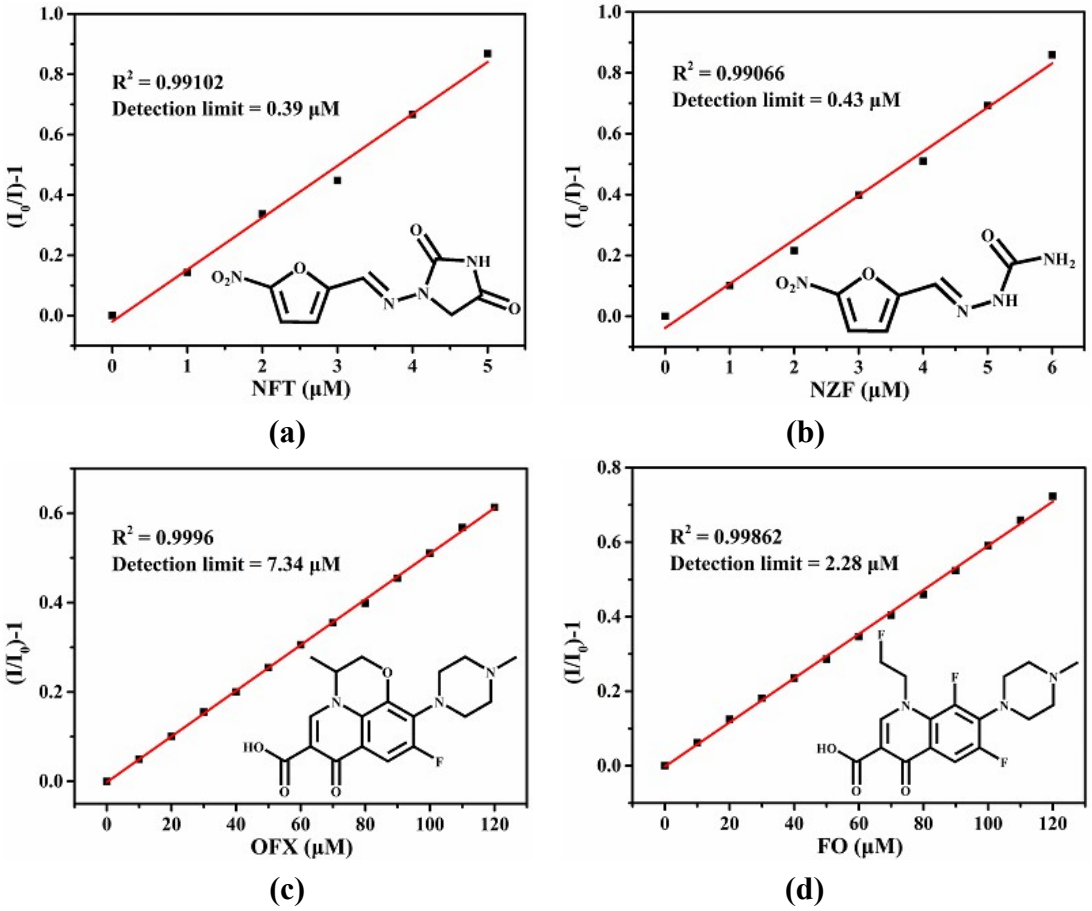

Fig. S10. The linear relationships between the fluorescence intensities of **JXUST-12a** and the concentrations of NFT (a), NZF (b), OFX (c) and OF (d) in aqueous solution.

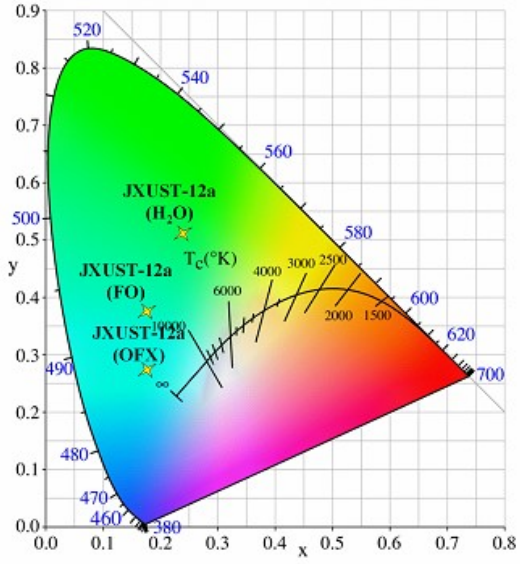

Fig. S11. CIE chromaticity diagram showing the color coordinates of **JXUST-12a** upon the addition of OFX and FO.

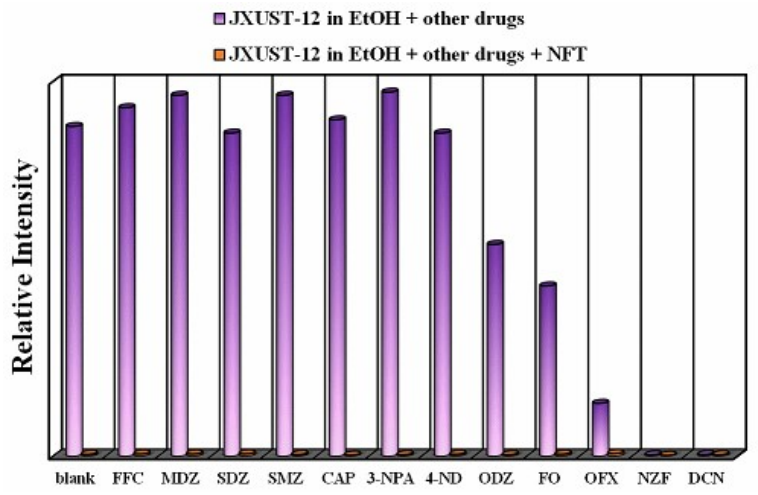

(a)

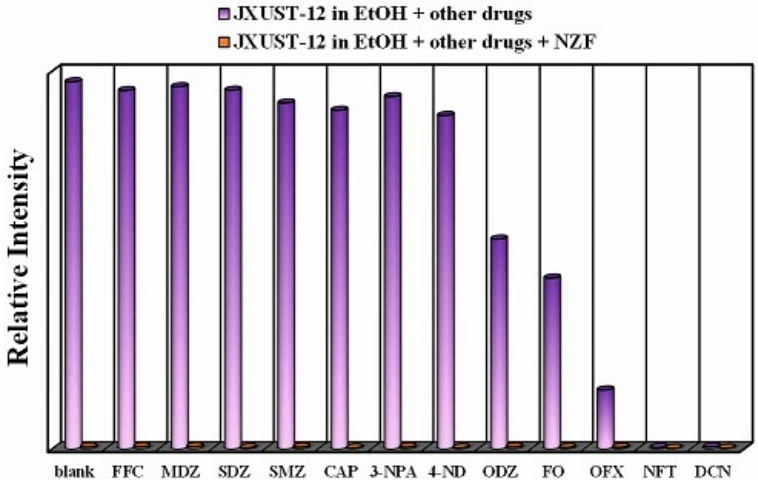

(b)

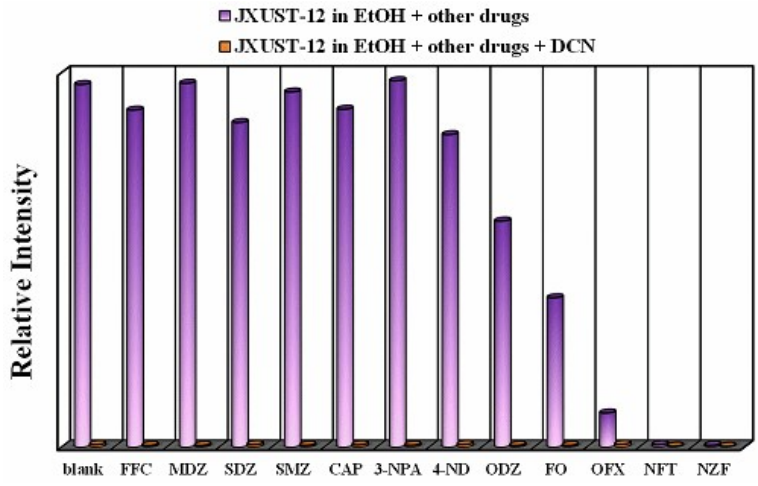

(c)

Fig. S12. Competitive experiments of **JXUST-12** in sensing NFT (a), NZF (b) and DCN (c) with the interference of other drug molecules (0.2 M) in EtOH solution.

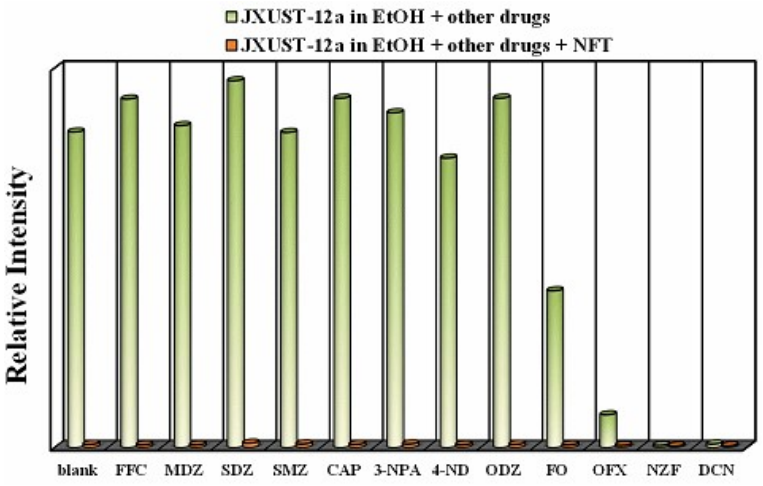

(a)

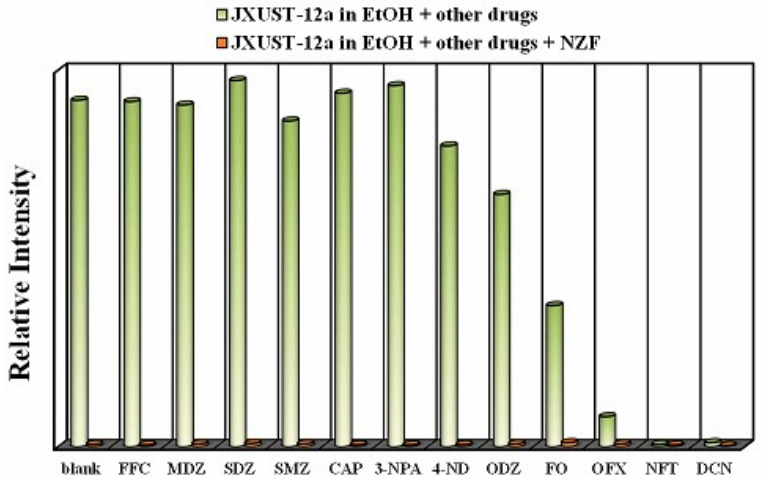

(b)

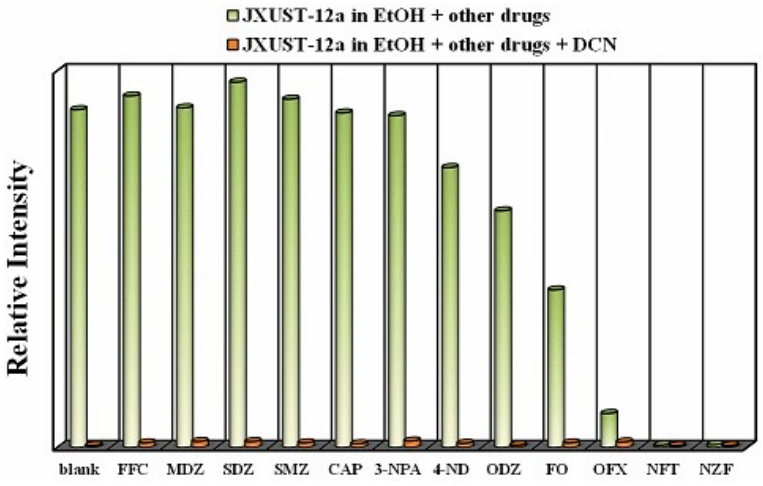

(c)

Fig. S13. Competitive experiments of **JXUST-12a** in sensing NFT (a), NZF (b) and DCN (c) with the interference of other drug molecules (0.2 M) in EtOH solution.

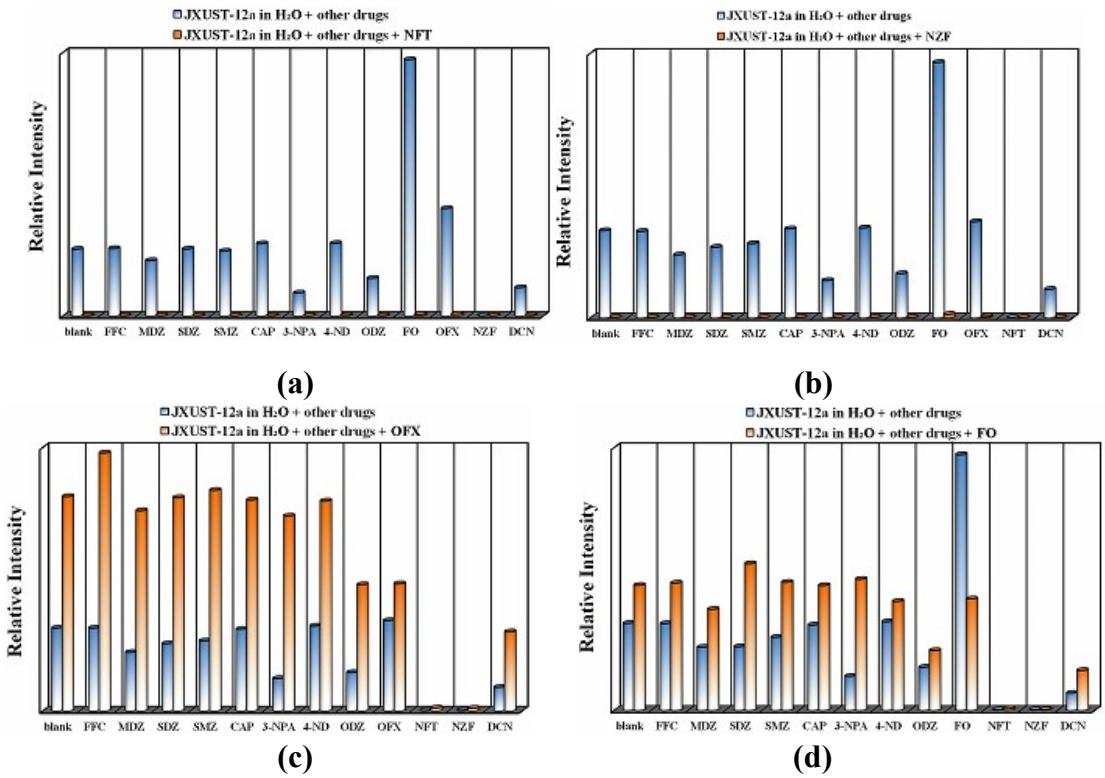

Fig. S14. Competitive experiments of **JXUST-12a** in sensing NFT (a), NZF (b), OFX (c) and FO (d) with the interference of other drug molecules (0.2 M) in aqueous solution.

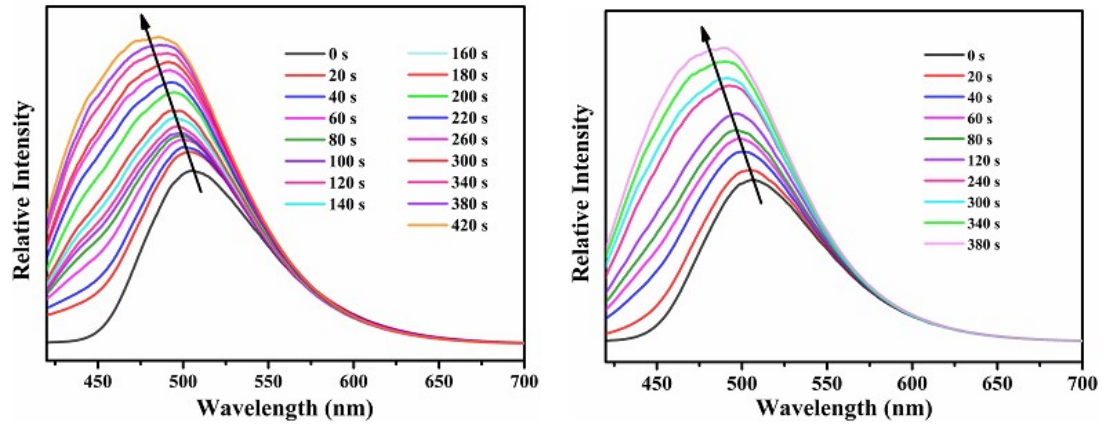

Fig. S15. Time-dependent emission spectra of **JXUST-12a** in aqueous suspension after adding OFX (a, 5×10^{-4} mol/L) and FO (b, 5×10^{-4} mol/L) at room temperature.

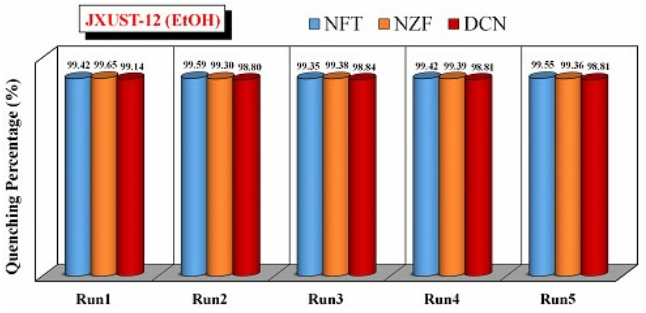

(a)

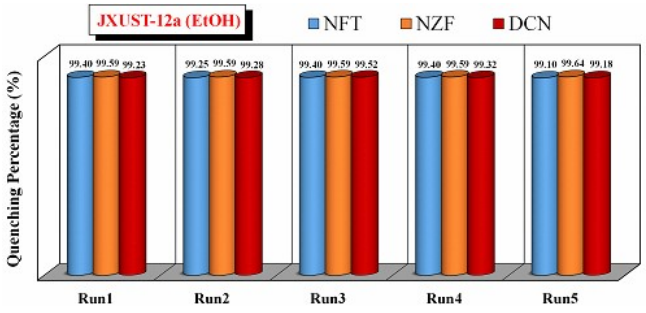

(b)

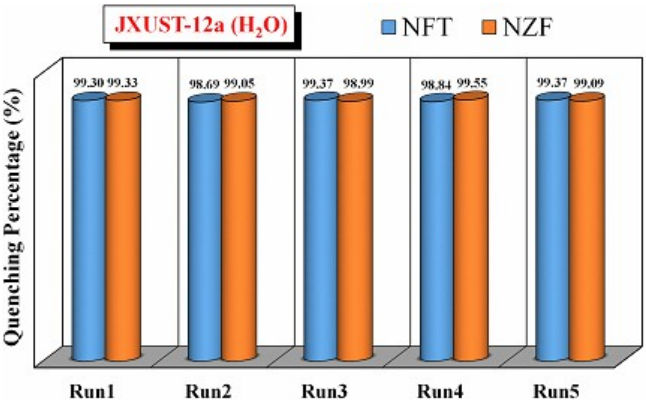

(c)

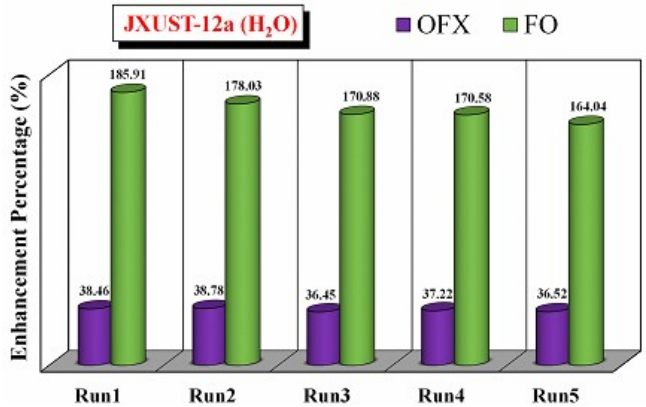

(d)

Fig. S16. Quenching efficiencies of **JXUST-12** (a) and **JXUST-12a** (b) in EtOH solution in the recyclable experiments for NFT, NZF and DCN; quenching efficiencies or enhancement efficiencies of **JXUST-12a** in aqueous solution in the recyclable experiments for NFT and NZF (c), and OFX and FO (d).

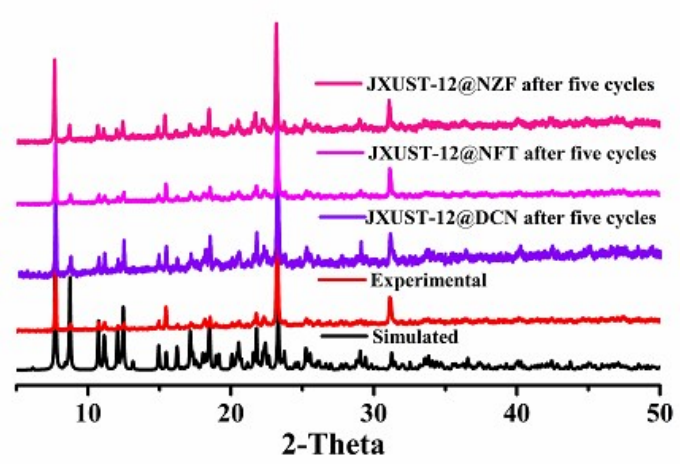

(a)

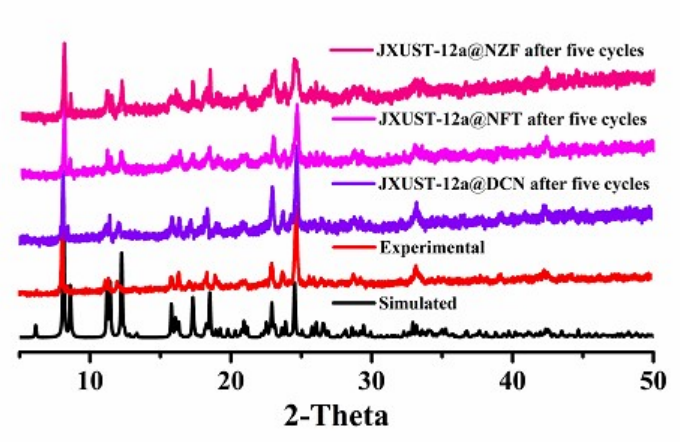

(b)

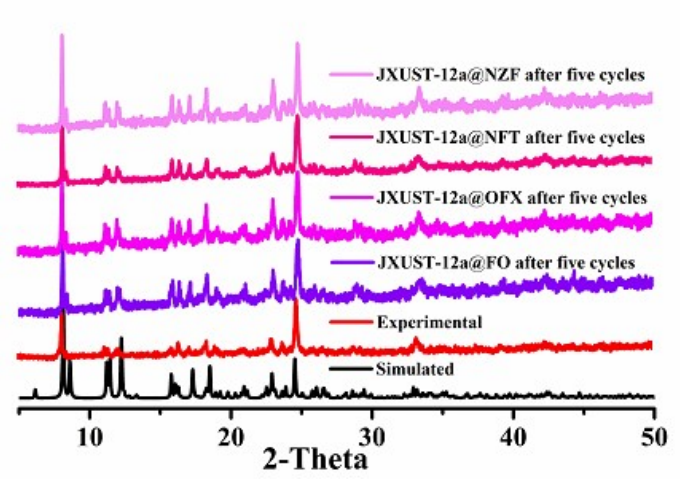

(c)

Fig. S17. The PXRD patterns of **JXUST-12** in EtOH solution (a), **JXUST-12a** in EtOH solution (b) and **JXUST-12a** in aqueous solution (c) after five cycles of fluorescence sensing.

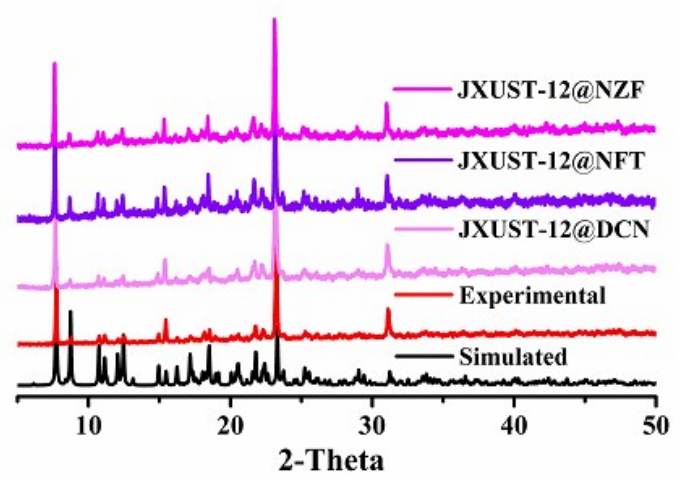

(a)

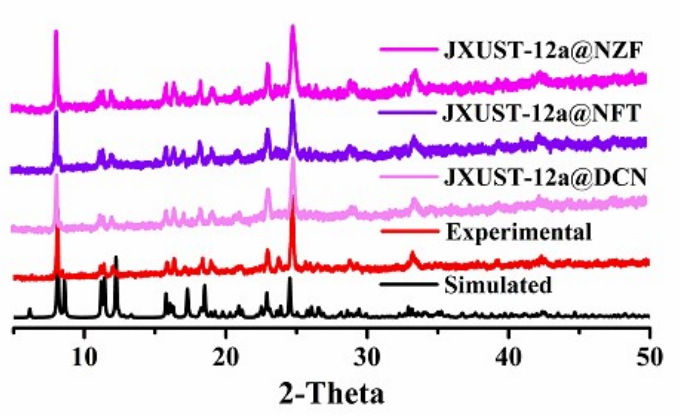

(b)

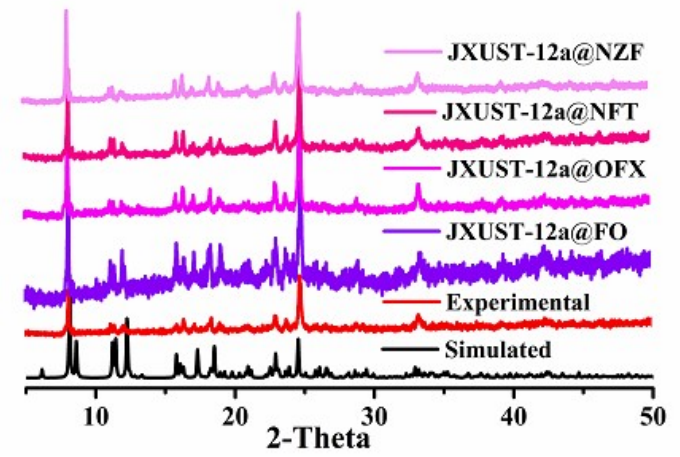

(c)

Fig. S18. The PXRD patterns of **JXUST-12** in EtOH solution (a), **JXUST-12a** in EtOH solution (b) and **JXUST-12a** in aqueous solution (c) after adding different drugs molecules.

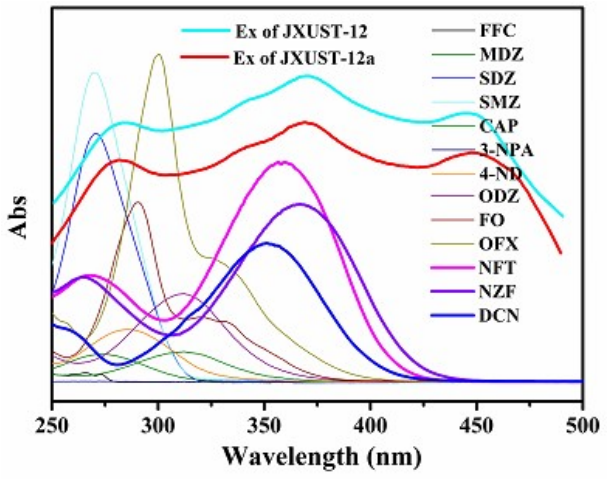

(a)

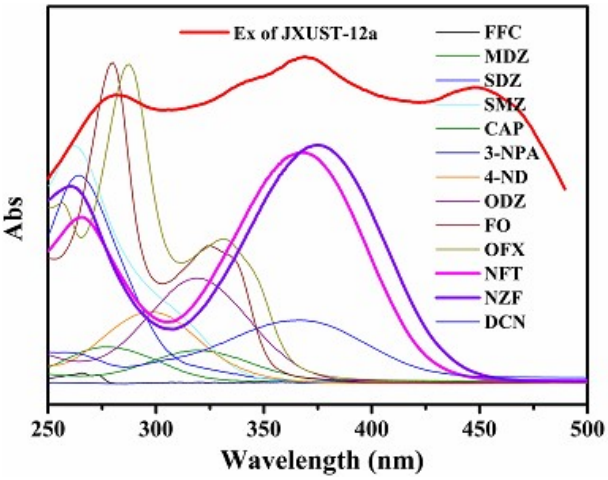

(b)

Fig. S19. The excitation spectra of **JXUST-12** and **JXUST-12a** in EtOH solution (a) and in aqueous solution (b) and UV-vis absorption spectra of all drug molecules.

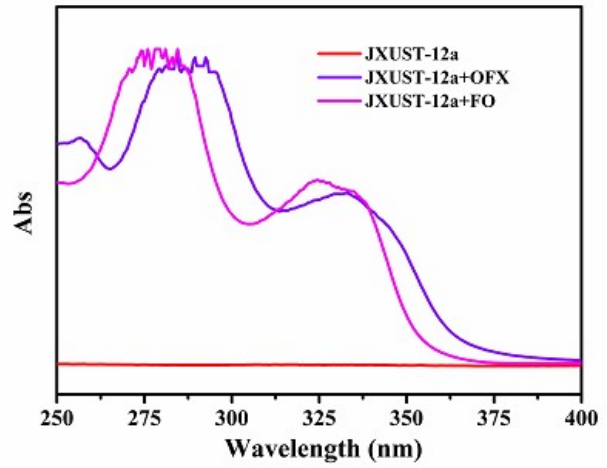

Fig. S20. The UV-vis absorption spectra of **JXUST-12a** and **JXUST-12a** upon the addition of OFX and FO.

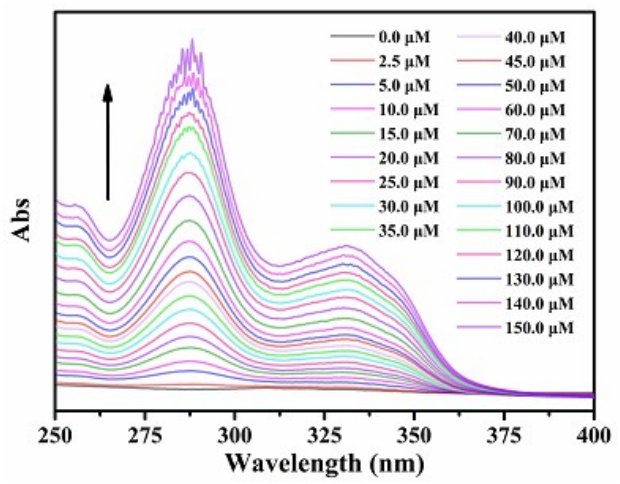

(a)

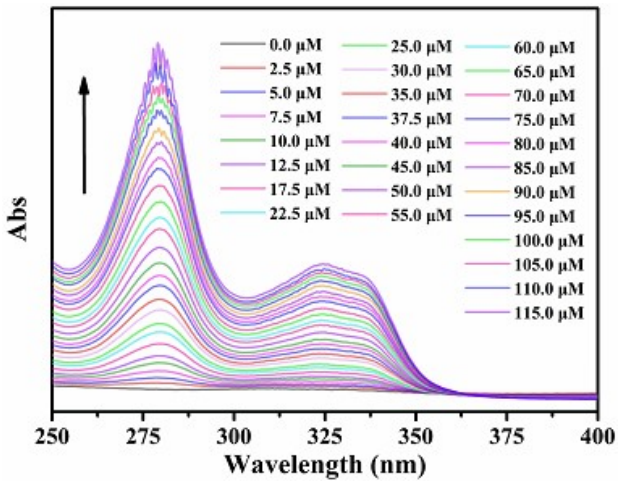

(b)

Fig. S21. The absorption spectra of **JXUST-12a** dispersed in aqueous solution after adding different concentration of OFX (a) and FO (b).